JOURNAL OF PROPULSION AND POWER
Vol. 14, No. 4, July–August 1998

Arcjet Anode Plasma Measurements Using Electrostatic Probes

Nicholas T. Tiliakos,* Rodney L. Burton,† and Herman Krier‡
University of Illinois at Urbana–Champaign, Urbana, Illinois 61801

A 1-kW hydrazine arcjet thruster has been modified for internal probing of the anode sheath boundary layer with an array of 14 electrostatic microprobes flush mounted into the anode body. Axial and azimuthal distributions of the plasma properties floating potential, anode sheath potential, wall current density, electron number density, and electron temperature have been obtained for arc currents between 7.8 and 10.6 A and propellant flow rates of 40–60 mg/s. The specific power ranged from 18.8 to 27.4 MJ/kg. Azimuthal symmetry has been verified for all arcjet operating conditions. The electron temperature data show that the near-anode plasma is highly nonequilibrium. Most of the current density and anode heating is located within 2–4 mm of the constrictor exit, with the location affected more by mass flow rate than by arc current. The axial anode heating distribution is closely coupled to current density and accounts for ~18–24% of the total input power. Reasonable agreement between a numerical model and experimental results is found for a constant value of the electron inelastic energy-loss factor.

Nomenclature

A_{eff} = effective probe collection area, m^2
A_p = geometric probe collection area, m^2
E = near-anode electric field, V/mm
E_{pl} = electric field in bulk plasma, V/mm
e = electronic charge, C
I = applied current to arcjet, A
$I_{e\text{-sat}}$ = electron saturation current, mA
I_p = total probe current, mA
j = current density, A/cm^2
j_a = anode current density, A/cm^2
j_{th} = thermal current density, A/cm^2
k = Boltzmann constant, J/K
L = nozzle axial length, mm
M_i = reduced N^+ and H^+ mass, kg
$\dot{m}$ = propellant mass flow rate, mg/s
m_e = electron mass, kg
n_{es} = electron number density, m^{-3}
n_r = number density of species r, m^{-3}
q_e = anode heating by electrons, W/cm^2
r_p = probe radius, mm
T = temperature, K
V = voltage, V
W = anode tungsten material work function, eV
α = degree of ionization
ε_i = ionization potential, eV
λ_D = Debye length, mm
λ_{rs} = mean free path, mm
λ_s = sheath thickness, μm
ϕ = potential, V

Subscripts
a = anode
arc = arcjet
e, i = electron/ion
f = floating
gas = plasma-gas flow
p = probe
s = presheath/plasma edge

Presented as Paper 97-3201 at the AIAA/ASME/SAE/ASEE 33rd Joint Propulsion Conference, Seattle, WA, July 6–9, 1997; received Sept. 30, 1997; revision received Dec. 11, 1997; accepted for publication Jan. 8, 1998.

*Ph.D. Candidate, Department of Aeronautical and Astronautical Engineering; currently Scientist, GASL, Inc., 77 Raynor Avenue, Ronkonkoma, NY 11779-6648. Member AIAA.

†Professor, Department of Aeronautical and Astronautical Engineering. Associate Fellow AIAA.

‡Professor, Department of Mechanical and Industrial Engineering. Fellow AIAA.

I. Introduction

ELECTROTHERMAL arcjet thrusters are now competitive with chemical propulsion systems for satellite station-keeping, maneuvering, and orbital transfer. To further improve arcjet performance, an understanding is needed of anode energy deposition q_e through experimentally validated numerical models. The q_e is mainly a result of the electron energy transferred from the arc to the anode, via the current attachment. It is suspected that anode wall loss is responsible for up to 50% of all losses in an arcjet, but to date, measurements have not been available.

This paper describes research conducted to improve the understanding of arc attachment and anode heating processes in the boundary layer of a 1-kW arcjet thruster operating on simulated hydrazine ($N_2 + 2H_2$) propellant.[1] An experimental investigation of an arcjet anode plasma boundary layer was performed with electrostatic microprobes, a type of Langmuir probe. A standard 1-kW arcjet design[2] was modified to accommodate 14 microprobes in the anode body, permitting analysis of anode heat transfer and validation of a numerical model.[3] Two main parameters were varied: 1) arcjet operating current from 7.8 to 10.6 A and 2) $N_2 + 2H_2$ propellant flow rate from 40 to 60 mg/s.

Langmuir probes have been employed for plasma diagnostics since the early 1920s, when the method was first developed and implemented.[4] The probe is a wire or sphere inserted into a plasma, biased positive or negative to collect charged particles. The resulting plot of probe current I_p vs probe voltage V_p yields information on plasma properties. Electrostatic probes have been used as an anode sheath diagnostic[5,6] and in electric thruster plumes.[7–11] They have also been used in supersonic and hypersonic flows.[12,13] The utility of electrostatic probes is not limited to cylindrical and spherical geometries only. Flush-mounted probes have been used for analyzing the properties in hypersonic flowfields.[14–18]

The first experimental investigations of the nozzle region of a low-power arcjet consisted of emission spectroscopy of the plasma flow inside the nozzle of a 1-kW hydrazine arcjet.[19] Additional investigations of plasma conditions inside the nozzle and constrictor have been performed on low- and medium-power arcjets.[20,21] Other internal diagnostic works have included internal emission spectroscopy measurements in the nozzle expansion region of a 26-kW ammonia arcjet.[22]

Curran et al.[23] studied arc energy deposition in the segmented anode of a 1- to 2-kW arcjet, the distribution of the arc attachment, and its effects on the performance characteristics of the device. The current to five anode segments, separated with boron nitride spacers, was individually measured along with the floating potential and anode fall voltage. Current was found to attach diffusely to the nozzle wall, with more than 50% in the diverging section of the nozzle. The current attachment distribution down the nozzle was found to be dependent on the mass flow rate, with the highest current density near the constrictor, consistent with previous results for electron number density.[18]

Determination of near-anode plasma properties aids in determining the transition between diffuse and constricted modes of arc attachment.[24] Operation of an arcjet in a constricted mode leads to high anode heating at the attachment point,[25] eventually limiting the electrode lifetime and decreasing thruster performance.[26] Knowledge of the current density distribution on the anode also aids in the validation of numerical models, as these models have had difficulty simulating the anode boundary-layer region. It was a goal of this work to provide data for model validation to aid in the design of advanced high-performance arcjet thrusters.

II. Experimental Approach

For this study a thruster was fabricated with similar dimensions to a standard 1-kW arcjet thruster[2] and modified to accept electrostatic probes. The thruster was operated at a simulated hydrazine flow rate of 40–60 mg/s, with a nominal current of 10 A, and 110 V across the electrodes. The specific power $P/\dot{m}$ ranged from 18.8 to 27.4 MJ/kg. The converging cone half-angle upstream of the constrictor was 30 deg, while the diverging section half-angle was 20 deg. The constrictor diameter of 0.63 mm and length 0.25 mm were kept identical to the standard arcjet, as was the axial cathode gap of 0.60 ± 0.13 mm. The exit plane diameter was 9.5 mm, providing an area ratio of 225:1.

The arcjet nozzle (anode) was fabricated from 2% thoriated tungsten. The cathode was also fabricated from 2% thoriated tungsten and had a 30-deg half-angle tip, with a diameter of 4.8 mm at the thruster head.

The major difference from the standard design was elimination of an anode insert and associated seal[2] and implementation of a single-piece thruster body. Use of a monolithic body facilitated modeling of the anode heat transfer, as well as placement of the array of 14 electrostatic microprobes at various axial and azimuthal locations in the anode wall (Fig. 1).

The probes were numbered to designate the axial distance (mm) from the constrictor exit. Probes 1, 4, 7, and 10 and probes 1′, 4′, 7′, and 10′ were at the same axial location, but separated azimuthally by 180 deg (Fig. 1). The remaining probes were located at 120 and 240 deg to provide information on current symmetry.

Microprobes 2–10′ were made from 0.43-mm-diam, 99.95% pure tungsten wire, surrounded by an alumina (Al_2O_3) insulator tubing (Fig. 2) with an o.d. of 0.86 mm and an i.d. of 0.51 mm, inserted into a type 304 stainless-steel support tube, with an i.d. of 1.22 mm. For probes 1 and 1′, 0.17-mm-diam tungsten wire was used, surrounded by an Al_2O_3 tube with an o.d. of 0.58 mm and i.d. of 0.20 mm, and inserted into a Type 304 stainless-steel support tube with an i.d. of 0.81 mm. The stainless-steel tube covers all but the last 2 mm of the probe, and so is not visible in Fig. 2.

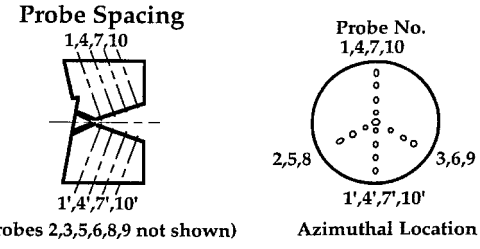

Fig. 1 Schematic of the array of 14 electrostatic microprobes flush mounted at millimeter-spaced axial locations. Probes 1, 4, 7, 10 and 1′, 4′, 7′ 10′ can be directly compared to verify current and plasma symmetry.

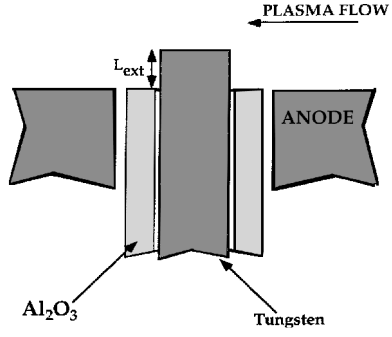

Fig. 2 Schematic of the tungsten probe–Al_2O_3 insulator configuration at the anode wall. The probe tip can extend a distance $L_{ext} \leq 0.3$ mm into the plasma flow; $L_{ext} = 0$ for this paper.

To summarize, 14 microprobes were located in the anode housing at 10 axial and 4 azimuthal locations downstream of the constrictor. The tungsten probe wire and alumina tubing were held in place with high-temperature (2200 K) zirconia adhesive. The wire probe tip could be extended into the plasma flow at various distances from the tubing end (Fig. 2). Tungsten was selected for the probe material because of its high melting point, and high work function (4.55 eV),[27] giving low electron emission. Further details regarding probe fabrication techniques are discussed in Ref. 1.

After each test, all probes were removed from the anode for inspection and re-measurement of their diameter. Data from visibly contaminated or eroded probes weres not included in the analysis. The probes were then abrasively cleaned and reused.

The thruster was mounted inside a 1.5-m^3 vacuum tank, with a background pressure range of 0.1–0.2 torr for flow rates between 40 and 60 mg/s. The $N_2 + 2H_2$ propellant flow rate was controlled by two Unit Instruments mass flow controllers. A radiation-shielded chromel–alumel type K thermocouple recorded nozzle surface temperature at 9.4 mm from the exit plane.

The plasma properties of floating potential, sheath potential, electron density, and temperature at the sheath edge, and anode current density were derived from the probe V–I characteristic,[1] obtained by biasing the probe with a sinusoidal function generator and measuring the probe current I_p with a 103.7-Ω current-sensing shunt resistor, recorded on a digital oscilloscope. The function generator frequency was 10 Hz to avoid distortion in the probe V–I characteristic, as well as unwanted voltage drops across the low inductance current-sensing resistor.

A. Probe Length Scales

The magnitude of the current to a biased probe depends on the sheath thickness and elastic and inelastic collisions in the sheath, and on the probe surface conditions, e.g., contamination, thermionic emission, and sputtering. Interpretation of the probe characteristic depends on the collisionality of the probe sheath. For no collisions in the sheath, n_{es} and T_{es} are obtained

from the electron current by subtracting the ion current from the total probe current.

To calculate the sheath length scales, a numerical arcjet model[3] was used to obtain values for n_H, n_H, n_{H_2}, n_{N_+}, n_N, n_{N_2} for the nominal conditions of $\dot{m}$ = 50 mg/s and I_{arc} = 10 A. These values were used to calculate Debye length and mean free paths at each probe location for 31 collisional reactions.[1] The mean free paths for the 31 separate collisional reactions were calculated using the cross-sectional data used in the numerical model.[3]

For ion collection probes 1–4′ were found to be highly collisional and probes 5–10′ were moderately collisional. For electron collection all of the probe sheaths were relatively collisionless. For both ion and electron collection the probe sheath was thin.[1] The effect of ion collisions is to reduce ion current to the probe, so that the slope of the electron current characteristic is increased, reducing electron temperature slightly.

B. Probe Collection Area

Whether the probes are flush mounted or extended partially into the flow, determining their geometric area is complicated if the alumina tubing is damaged, exposing an additional collection area. Damage to the alumina was almost exclusively confined to probes 1, 1′, and 2, located in the region of maximum current density, and was characterized by cracking or vaporization of the Al_2O_3 tubing caused by intense heating and thermal stresses, which exposed more probe surface to the plasma flow. When damage occurred the probe area was calculated by averaging the pretest and posttest A_p values. The posttest geometric probe area was given as[1]

$$A_{posttest} = \pi D_p^2/4 + \pi D_p c \bar{L} \tag{1}$$

where D_p is the probe diameter, c is the fraction of Al_2O_3 tip cracked, and $\bar{L}$ is an average probe exposure length caused by Al_2O_3 cracking. The values for D_p, c, and $\bar{L}$ are based on posttest visual observations of each probe with a magnifying lens.

The sheath surrounding the probe creates an effective collection area A_{eff} that is somewhat larger than A_p. Accounting for the sheath is particularly important if the probe bias is high, in which case the probe sheath may extend far enough into the boundary layer that convection effects must be included in the analysis of the probe characteristic.[1,28]

When λ_s is comparable to the probe dimensions, the sheath is termed thick and the probe effective collection area is appreciably larger than the physical area of the probe. Based on calculations of the sheath thickness for all 14 probes,[1] the sheath effect increased the probe collection area by a maximum of 10%.

C. Probe Damage and Contamination

Contamination of the probe surface can severely distort the probe V–I characteristic, leading to erroneous results in j_a, T_{es}, and n_{es}.[29] If the probes are clean then the current for probes at the same axial location should be equal. However, the signal from a contaminated probe is much less than from a clean probe and a contaminated probe has an altered characteristic slope, resulting in a spuriously high T_{es} measurement.

Once a probe was contaminated in situ it was very difficult to clean and was replaced. The greatest chances for probe contamination to occur were within the first 1–2 min of arcjet startup before attaining a steady arcjet operating voltage, and when the probes collected too much current during cleaning, causing melting of the Al_2O_3 tip.

In this work, the probes were maintained in a clean state using a pulsed ion bombardment technique, in which the probes were sequentially cleaned with 1–2 square-wave pulses of negative 160-V amplitude, with a duration of about 0.15 s. The cleaning efficiency was found to be relatively insensitive to the probe cleaning voltage, the cleaning pulse duration time, the number of cleaning pulses, and the probe diameter.[1]

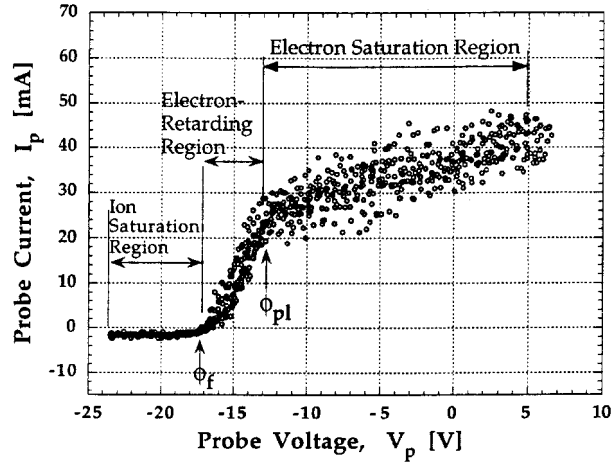

Fig. 3 Typical probe V–I characteristic curve with regions of interest indicated.

D. Typical Probe V–I Characteristic

A typical probe V–I characteristic is shown in Fig. 3 for $P/\dot{m}$ = 22 MJ/kg. The floating potential ϕ_f, plasma potential ϕ_{pl}, ion and electron saturation regions, and electron-retarding regions are shown. The plasma potential is measured at the intersection of the electron-retarding and saturation regions, and is 24 ± 5 V in Fig. 3. The electron current slope in the electron-retarding region, after a small correction for ion current,[1] provides a measure of the electron temperature T_{es} at the presheath/plasma edge.[30] The electron number density is derived from knowing the probe current at ϕ_{pl}, T_{es}, and A_p.[30]

III. Experimental Results

Table 1 summarizes the steady-state thruster operating conditions using flush probes. Results with probes extended up to 0.3 mm into the flow were similar to those of the flush probes.[1]

A. Floating Potential Distribution

Figure 4 presents the measured floating potential distributions along the anode wall for four operating conditions. It was observed that regardless of these conditions the floating potential data for the 120- and 240-deg probes lie on the same curve as the 0- and 180-deg probes, implying azimuthal symmetry.

As the propellant flow rate increases, i.e., $P/\dot{m}$ decreases for fixed I_{arc}, the floating potential becomes more negative, with azimuthal symmetry at all conditions. At all flow rates studied there is an absolute maximum in floating potential between 2 and 3 mm; for $x > 3$ mm, ϕ_f monotonically approaches 0 V. This result is consistent with high T_{es} between 2 and 3 mm, so that a larger probe potential is required to maintain $j_p = 0$ for a floating probe. Likewise, as the plasma flow expands through the nozzle, the electron temperature decreases, so that a smaller ϕ_f is required.

Keeping $\dot{m}$ constant and varying I_{arc} from 7.8 to 10.6 A produces very little effect on the ϕ_f distribution. The observed variation is within the experimental error of ±1 V, except for a variation of ±2.5 V at x = 2 mm.

B. Anode Sheath Potential Distribution

The anode sheath potential ϕ_s is also derived from the probe V–I characteristic, and is the negative of ϕ_{pl},[31] where ϕ_{pl} is determined by the intersection of the electron-retarding and electron saturation regions of the V–I curve (Fig. 3).

An expression can be written for anode sheath potential that provides an estimate of the electron temperature[1,32]:

$$\phi_s = -\phi_f + (kT_{es}/e)\{\ell n(\alpha_c) + \ell n[0.61\sqrt{(2\pi m_e/M_i)}]\} \tag{2}$$

Table 1 Summary of steady-state arcjet thruster operating conditions

Operating condition	$\dot{m}$, mg/s	Average I_{arc}, A	Average V_{arc}, V	Power, W	$P/\dot{m}$, MJ/kg	T_e, K
a	40	10.6	104	1102	27.4	945
b	45	9.8	109	1068	23.6	935
c	50	7.8	121	944	18.8	870
d	50	8.9	115	1023	20.6	900
e	50	9.8	112	1098	22.0	910
f	60	9.9	121	1198	20.0	895

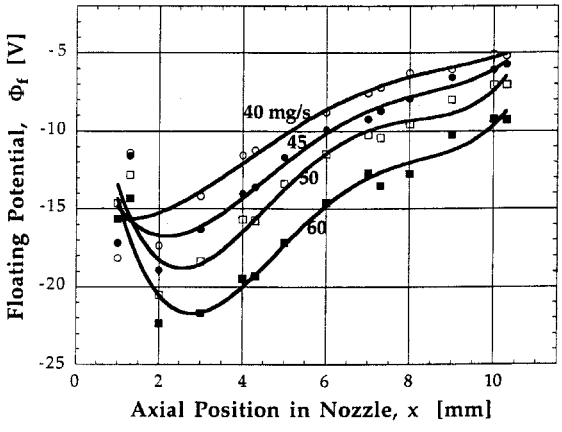

Fig. 4 Floating potential data for 45, 50, and 60 mg/s, 9.9 A, and 40 mg/s, 10.6 A. Typical arc voltage is V_{arc} = 104 V. The error on the floating potential is ±1 V, with error bars were omitted for clarity.

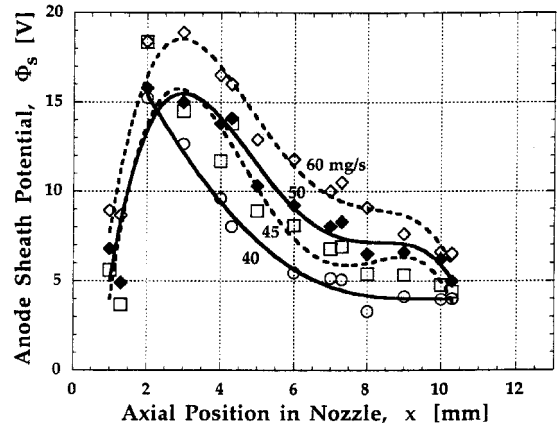

Fig. 5 Sheath potential for 45, 50, and 60 mg/s, 9.9 A, and 40 mg/s, 10.6 A. In all cases the sheath is electron attracting because $\phi_s > 0$. The error in the sheath potential is ±1 V.

where

$$\alpha_c \equiv \left[1 + \frac{\pi\lambda_D}{2\lambda_{H^+-H_2}}\right]^{-1/2}$$

Eq. (2) is valid when both the probe sheath and presheath are collisionless and derives from the floating probe condition $j_i = j_e$.

The effect of propellant flow rate on the anode sheath potential distribution is shown in Fig. 5. As the propellant flow rate is increased from 40 to 60 mg/s, ϕ_s increases at all probe locations and the maximum in the ϕ_s axial profile distribution shifts from probe 2 to probe 3.

For flow rates of 40–50 mg/s an absolute maximum exists in the sheath potential at about x = 2 mm, similar to the ϕ_f data. In all cases ϕ_s decreases monotonically for $x \geq 2$ mm. Throughout the anode boundary layer $\phi_s > 0$, so that the anode sheath is always electron attracting.

C. Current Density Distribution

The current density j_a is evaluated by averaging the digital samples of probe current over a range of ±0.1 V centered at 0 probe volts. Figure 6 shows the current density for 45, 50, and 60 mg/s at 9.8 A, and for 40 mg/s at 10.6 A.

1) The current density j_a decreases monotonically with x, except for 60 mg/s and 9.8 A, where j_a peaks at 3 mm.

2) For $\dot{m}$ = 40, 45, and 50 mg/s the current density is maximum at 1 mm. The current density decreases from 38 ± 11.5 A/cm^2 near the constrictor to ~3.0 ± 0.6 A/cm^2 at 10 mm.

3) For most of the experimental conditions studied, azimuthal current symmetry is inferred from the j_a data obtained, within experimental error. The exception is a discrepancy between probes 1 and 1′.

At 40 mg/s, probe 1 gives a current density five times larger than 1′. The discrepancy decreases from 42% at 45 mg/s to 36% at 50 mg/s and to 24% at 60 mg/s. Some of this uncertainty is ascribed to the uncertainty in the probe collection area, [© ~ (15—35%)] as the probes adjacent to the constrictor experienced the highest thermal stresses, damaging the alumina insulator.

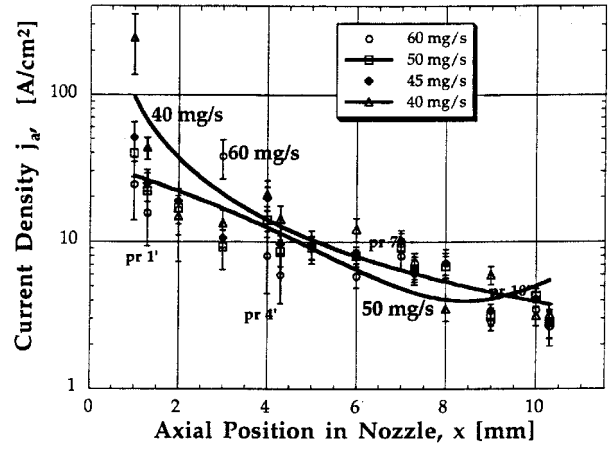

Fig. 6 Current density distribution along the anode for 45, 50, and 60 mg/s, 9.8 A, and 40 mg/s, 10.6 A.

4) The most significant change in the current density distribution occurs for 60 mg/s, for which the current density peak shifts downstream to x = 3 mm. Based on the $\dot{m}$ and I_{arc} parameter studies it appears that $\dot{m}$ affects the j_a distribution more than I_{arc} with regard to the location of maximum current density.

A weighted anode sheath potential is calculated as

$$\bar{\phi}_s = \int_0^L j_a(x)\phi_s(x)\, dA(x) \Big/ I_{arc} \qquad (3)$$

where x is in mm, $j_a(x)$ is the current density distribution, and $\phi_s(x)$ is the anode sheath potential distribution. For the $j_a(x)$ and $\phi_s(x)$ distributions the values for the 0- and 180-deg probes are averaged to obtain a single data point in Eq. (3).

The weighted anode sheath potential as a function of propellant flow rate exhibits a minimum at 50 mg/s and 9.9 A, increasing for $\dot{m} \geq 50$ mg/s. The largest value for $\bar{\phi}_s$, 17 ± 5.1 V, occurs at 60 mg/s and $P/\dot{m}$ of 19.9 MJ/kg. Similarly, for 40 mg/s and 27.4 MJ/kg, $\bar{\phi}_s$ has a low value of 8.1 ± 1.6 V. The results agree in general with Curran et al.,[23] who found that the anode fall voltage was on the order of 10–20 V.

D. Electron Number Density

Figure 7 presents the electron number density results for 60, 50, and 45 mg/s at 9.8 A, and 40 mg/s at 10.6 A. For all flow rates studied, n_{es}, which ranges from $\sim 10^{18}$ to 10^{19} m^{-3}, is largest at 1 mm with a secondary peak at 4 mm, and decreases down the nozzle. For all cases the axial variation of n_{es} varies from 3.5–10 × 10^{18} m^{-3} at 1 mm, to 7–10 × 10^{17} m^{-3} at 10 mm.

Symmetry in the n_{es} data is reasonable for all flow rates except 45 mg/s, where the largest n_{es} difference between the 0- and 180-deg probes is 60%, for probes 1 and 1′ only. This corresponds to the symmetry observed earlier for the j_a data at the same conditions.

In the region of attachment of 2–4 mm, n_{es} increases with increasing $P/\dot{m}$ and fixed I_{arc}; as $P/\dot{m}$ increases 38% n_{es} increases by 74%. For $x > 5$ mm, increasing $P/\dot{m}$ does not have as large an effect on the n_{es} distribution.

E. Electron Temperature

T_{es} at the presheath/plasma edge, coupled with the ϕ_s and j_a results, is needed to estimate q_e. In addition, T_{es} allows the calculation of scalar electrical conductivity σ and thermal conductivity κ in the anode boundary layer.

The T_{es} distribution is derived from the classical V–I characteristic method, using the inverse slope of the electron-retarding region. However, as will be shown later in this paper, different results were obtained from the sheath potentials [Eq. (2)].

Electron temperatures derived from the V–I slope method are plotted in Fig. 8 for three values of mass flow rate at 9.8 A. For all mass flow rates T_{es} was highest from 1–3 mm, at 30,000 ± 5000 K, falling to 16,000 ± 4000 K farther from the constrictor.

The symmetry in the T_{es} data for the 0- and 180-deg probes at 1, 4, 7, and 10 mm is reasonably good, particularly at 50 and 60 mg/s. For 45 mg/s the T_{es} data for probes 1, 1′ and probes 7, 7′ differ by about 32%.

For all propellant flow rates tested, the ratio T_{es}/T_g is much greater than unity in the near-anode region, at all probe locations, because $T_e > 10{,}000$ K is required to maintain the electrical conductivity. For a gas temperature of 1400 K, slightly greater than that of the anode wall, $T_{es}/T_g \sim \mathcal{O}(7\text{–}20)$. This value for the gas temperature is reasonable because nozzle surface temperature measurements yield $T_{noz} \sim 950$ K and the numerical model predicts $T_{gas} \sim 1200$ K along the anode wall. This strongly suggests that a nonequilibrium two-temperature plasma exists in the near anode region of the arcjet.

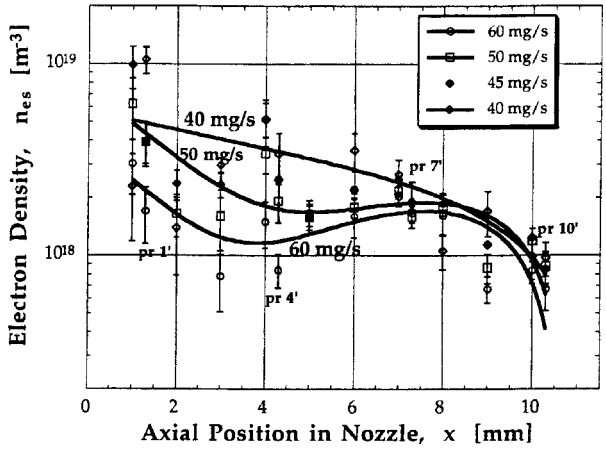

Fig. 7 Electron number density distribution along the anode for 45, 50, and 60 mg/s, 9.8 A, and 40 mg/s, 10.6 A.

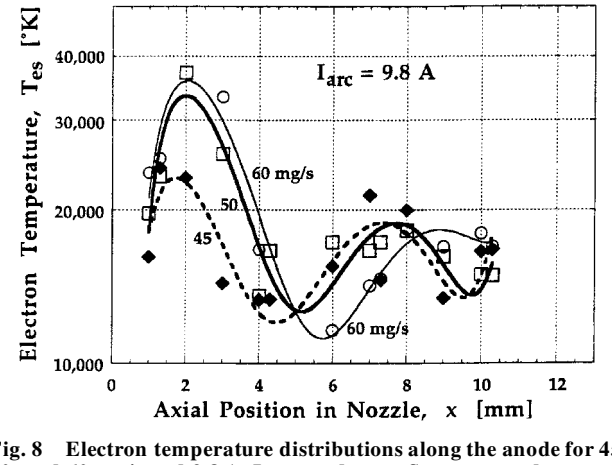

Fig. 8 Electron temperature distributions along the anode for 45, 50, and 60 mg/s and 9.8 A. Increased mass flow rate tends to push the distribution downstream.

F. Anode Heating

The electron energy deposition in the anode sheath was studied as a function of $\dot{m}$, I_{arc}, and $P/\dot{m}$. The energy deposition into the anode for an electron-attracting sheath is calculated from[1,33]

$$q_e = j_a(5kT_{es}/2e + \phi_s + W) \tag{4}$$

where the first term in the parentheses represents the thermal energy of the electrons, the second term is the electron energy gained in traversing the sheath, and the last term is the energy gained when the electron recombines with the anode surface. The work function W of the 2% thoriated tungsten anode is 3.7 eV, an average value between that for 2% thoriated and pure tungsten.[27] The plasma properties j_a, n_{es}, and T_{es} vary with propellant flow rate, arcjet operating current, and specific energy, affecting anode heating through Eq. (4).

It was stated earlier that the location of maximum j_a was more sensitive to the mass flow rate than to the arcjet operating current. The effects of propellant flow rate on anode heating are shown in Fig. 9 for $\dot{m}$ = 45 and 50 mg/s at 9.8 A, and 40 mg/s, at 10.6 A, using flush-mounted probes.

There is a minimal difference in the q_e distribution for 40, 45, and 50 mg/s. Results for these flow rates show a peak in

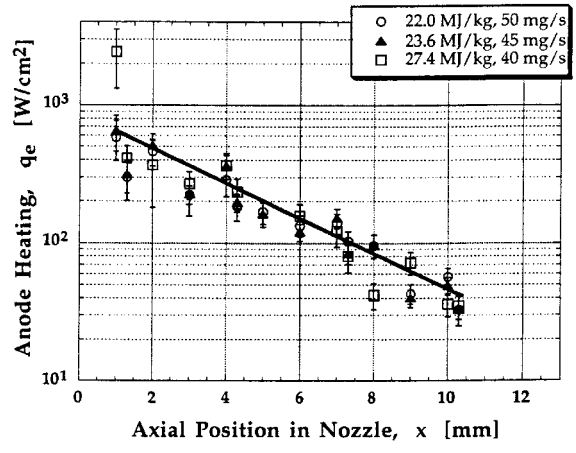

Fig. 9 Anode heating distribution q_e for 40, 45, and 50 mg/s, 10 A.

q_e at 1 mm (Fig. 9), with a minor secondary peak at $x = 4$ mm, similar to the j_a distribution. As with the j_a results, when $\dot{m}$ is increased to 60 mg/s, $(q_e)_{max}$ is displaced downstream to 3 mm, again coinciding with $(j_a)_{max}$. Thus, the peak in anode heating is a function of the current density and both are dependent more on the propellant flow rate than on I_{arc}. For 45 mg/s the anode heating varies from approximately 480 W/cm^2 at 1 mm to 41 W/cm^2 at 10 mm. Similarly, for 50 mg/s, q_e varies from 440 ± 140 W/cm^2 at 1 mm to 40 ± 8 W/cm^2 at 10 mm.

The q_e distribution for the highest specific power tested, 27.4 MJ/kg (40 mg/s, 10.6 A) gave a heat flux of 1420 ± 600 W/cm^2 at 1 mm, the largest value obtained for all flow rates tested. This coincides with the largest current density obtained, 140 ± 57 A/cm^2 at $x = 1$ mm, for the same operating conditions. For all propellant flow rates studied, $q_e(x)$ monotonically decreases after $(q_e)_{max}$, a trend also observed in the current density distribution.

The total electron energy power deposition to the anode Q_a is written for an electron-attracting sheath as

$$Q_a \equiv \int_0^L \bar{q}_e(x)\, \mathrm{d}A(x) = \int_0^L j_a \left(\frac{5kT_{ex}}{2e} + \phi_s + W \right) \mathrm{d}A(x) \qquad (5)$$

where $\mathrm{d}A(x) = 2\pi r(x)(\cos 20\ \mathrm{deg})^{-1}\, \mathrm{d}x$. For the 0- and 180-deg probes an average value is used for $q_e(x)$ at $x = 1$, 4, 7, and 10 mm.

Using measured values the electron energy deposition in the anode ranged from 18–24% of total arcjet power, for 18.8–27.4 MJ/kg. These fractional energy values agree well with previous results in experiments with a water-cooled arcjet simulator,[34] for which the percentage of the total power lost to the anode was 20–25% of the total input power.

For a fixed 50 mg/s, Q_a was a maximum of 229 ± 49 W (22% of input arc power) at $I_{arc} = 8.9$ A, then decreased to 197 ± 42 W (18% of arc power) as I_{arc} was increased to 9.8 A. For increasing flow rate at fixed current, Q_a varied from 18% of the total input power for 50 mg/s and 9.8 A to 287 ± 60 W (24% of arc power) for 60 mg/s and 9.9 A. Thus, the maximum anode heating occurred for the highest propellant flow rate, indicating that when operating the arcjet at low specific power, a larger fraction of the total input power is absorbed into the anode.

G. Plasma Properties

Once the electron temperature and number density distributions are known, plasma transport properties such as scalar electrical conductivity can be calculated along the anode. The degree of ionization α for this multispecies plasma is defined as

$$\alpha_{ioniz} \equiv \frac{n_e}{n_{H_2} + n_{N_2} + n_H + n_N} \approx \frac{n_e}{n_{H_2} + n_{N_2}} \qquad (6)$$

For 50 mg/s and 9.8 A, based on the measured n_e and predicted n_{H_2} and n_{N_2} from a numerical model,[3] α_{ioniz} varies from 7×10^{-6} at 1 mm to 3×10^{-5} at 5 mm to 8×10^{-5} at 10 mm. In this range of α_{ioniz} the electrical conductivity is dominated by electron-neutral collisions.

H. Comparison with Previous Experiments

The only previously published current density measurements in a low-power hydrazine arcjet were by Curran et al.,[23] operating a 1-kW arcjet. The main findings were that the total current had minimal effect on the measured current distribution, the propellant flow rate had a strong effect on the current distribution, the anode fall was found to be between 10 and 20 V, and for $\dot{m} = 49.7$ mg/s and 10 A, approximately half of the total operating arcjet current was collected on the segment closest to the nozzle exit, within 5 mm of the exit plane. Because of the segmented geometry no conclusions could be reached with respect to symmetry and anode heating.

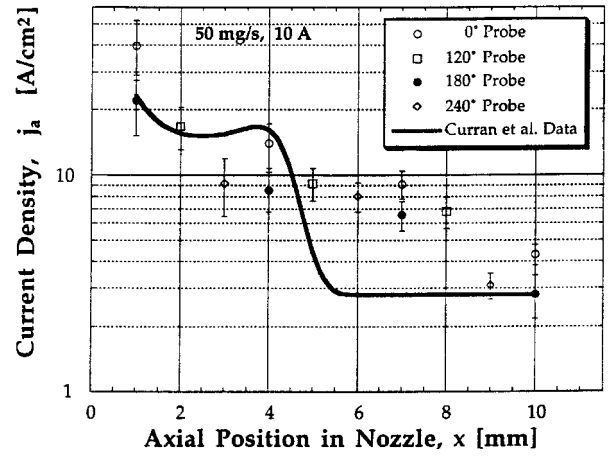

Fig. 10 Comparison for 50 mg/s, 10 A between current density measurements and segmented anode data of Ref. 23.

The results of this work generally agree with these findings. Figure 10 shows a comparison between the flush probe current density data for 50 mg/s and 9.8 A ($P/\dot{m} = 22$ MJ/kg), and the data of Ref. 23, for 49.7 mg/s and 10 A ($P/\dot{m} = 27$ MJ/kg). The experimental data in Fig. 10 compare reasonably well, even with a 16% difference in arcjet operating voltage and a 20% difference in $P/\dot{m}$. The largest difference between the two experiments occurs at 1 mm and in the anode region at 5–8 mm. At 1 mm, Ref. 23 data lie between the results of probes 1 and 1′, though much closer to probe 1′. For 5–8 mm the Ref. 23 current density measurements give 2.9 A/cm^2, compared to 7–9 A/cm^2 measured here. Both sets of data display a maximum current density at 1 mm, with a smaller secondary peak at 4 mm.

I. Comparison with Numerical Model

An important recent advance has been the simulation of arcjet physics with multifluid nonequilibrium models.[3,35] The Megli–Krier–Burton model[3] employed here provides a self-consistent approach to solving Ohm's law and the particle energy equations, which are coupled to the equations of chemical nonequilibrium kinetics, the Navier–Stokes equations, and Maxwell's equations with appropriate boundary conditions. The model assumes steady-state, laminar flow, and includes injection flow swirl and anode heat transfer in a converging–diverging nozzle geometry with variable cathode arc gap. It also includes a variable-nozzle geometry, a variable mixture of nitrogen and hydrogen, and accounts for the chemical kinetics of seven species: H_2, N_2, H, N, H^+, N^+, and e^-.

The model's electron energy equation accounts for inelastic losses to molecular internal energy modes, i.e., rotational, vibrational, excitational, and ionization, through multiplying the electron–molecule collision frequencies by an energy loss factor δ. The δ factor is strongly dependent on the collision partner and T_e, and weakly on the gas temperature T_g.[3]

Large uncertainties are found in the literature for δ of various molecules.[3,36,37] The selection of a proper energy loss factor strongly affects the model arc attachment location and the electron temperature and density populations near the anode wall.

The model results were compared with experimental flush-probe current density data for the nominal arcjet conditions of 50 mg/s and 9.8 A. Numerical results for a variable locally adjusted variable δ, δ = 1200, and δ = 3000 are shown in Fig. 11. There, is reasonably close agreement between experimental results and the δ = 1200 and 3000 cases. The δ = 1200 case provides better agreement than δ = 3000 within 2 mm of the constrictor exit, where the axial current density gradient is

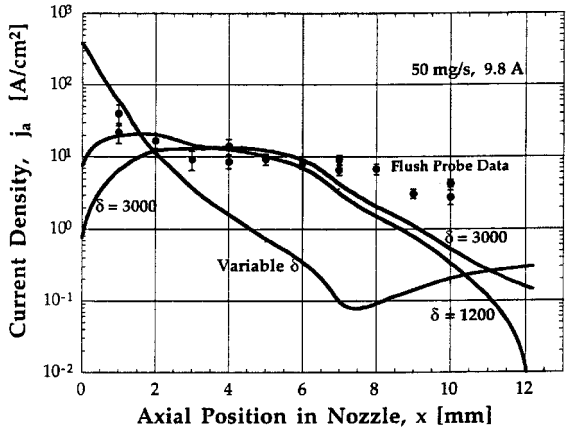

Fig. 11 Comparison of experimental and numerical results for wall current density, for 50 mg/s and 9.8 A. The numerical model assumes both variable δ and constant δ = 1200 and 3000.

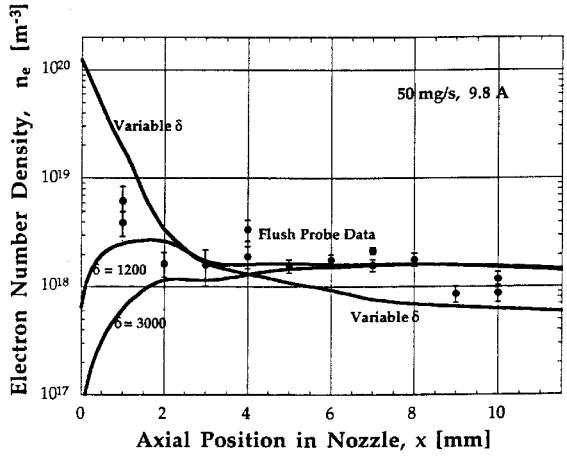

Fig. 12 Comparison of experimental and numerical results for wall electron density, for 50 mg/s and 9.8 A. The numerical model assumes both variable δ and constant δ = 1200 and 3000.

largest. Agreement between the experiment and the variable δ model is poor.

These results imply that an accurate accounting of inelastic energy losses in the anode sheath layer is important for realistic simulation of current attachment. The best agreement in the arc attachment zone, 2–6 mm, is obtained with δ = 1200 or 3000. A better fit to the experimental data is obtained at probes 1 and 1′ using δ = 1200. Obtaining good agreement between the model and the experimental data in the arc attachment zone is important because most of the anode heating occurs there.

As with current density, the predicted electron number density distribution $n_{es}(x)$ in the anode sheath layer is dependent on the δ factor. Figure 12 shows n_{es} at all probe locations for 50 mg/s and 9.8 A, compared with the model for variable δ and δ = 1200 and 3000.

As with the current density predictions, reasonable agreement between experiment and δ = 1200 and 3000 exists for the region 2–10 mm, with δ = 1200 providing a better fit to the experiment at 1 mm.

As discussed, $T_{es} >> T_g$ near the anode wall, so that a high degree of thermal nonequilibrium exists in the anode boundary layer. This condition results in an elevated population of charged species,[3] permitting the conduction of electrical current through the relatively cold gas layer adjacent to the anode.

Figure 13 shows experimental electron temperature determined by two different methods for 50 mg/s and 9.8 A, compared with the model results with variable and constant δ factors. Higher values of T_{es} are obtained with the V–I slope method, and lower values with the $\phi_f - \phi_s$ method. Both methods agree at 1 mm, but predict T_{es} = 22,000 K vs 12,000 K from the model. The δ = 1200 and 3000 cases predict a maximum electron temperature at x = 2 mm, in agreement with the V–I method. The model and both experimental methods show that the electron temperature decreases for x > 2 mm, and all results predict $T_{es} >> T_g$.

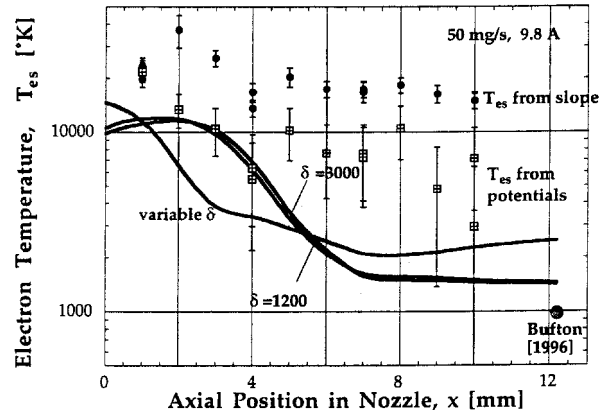

Fig. 13 Comparison of experimental and numerical results for wall electron temperature for 50 mg/s and 10 A. The numerical model assumes both variable δ and δ = 1200 and 3000. The exit plane data point was obtained from Ref. 8. Better agreement with the model is obtained for T_{es} derived from sheath and floating potentials than from the slope of the V–I characteristic.

Both T_{es} methods, V–I slope and $\phi_f - \phi_s$, assume that the electron sheath is thin and collisionless with the electrons exhibiting a Maxwellian distribution. The electron temperature based on the slope appears to be more sensitive to probe contamination, which artificially reduces the slope, raising the calculated T_{es}. It has been observed that even when a probe is clean, hysteresis is sometimes present on the probe V–I characteristic, introducing uncertainty in the analysis.

Using the electron temperature based on the V–I slope method leads to calculations of j_a which, when integrated over the internal anode surface area, result in 10 ± 2.5 A, reasonably close to the I_{arc} value. Using T_{es} based on the $\phi_f - \phi_s$ method results in I_{arc} = 8 ± 2 A. However, Fig. 13 shows better agreement between the model T_{es} results and T_{es} based on the $\phi_f - \phi_s$, when compared with the V–I slope method.

In summary, it is difficult to determine which method of evaluating T_{es} is better or preferable. The probe V–I characteristic indicates a Maxwellian distribution for the electrons, suggesting that extracting a temperature by this method is appropriate. However, T_{es} based on the plasma potential measurements shows better agreement with the numerical model. The experimental data are also more consistent with measurements by Bufton in the arcjet exit plane,[8,9] as shown in Fig. 13.

IV. Conclusions

Internal arcjet diagnostics experiments were conducted using 14 electrostatic microprobes flush mounted in the anode of a 1-kW arcjet thruster operating on simulated hydrazine and compared with a numerical model. It was shown that useful plasma measurements can be obtained with this diagnostic tool in the harsh environment of an arcjet.

Principal conclusions are as follows:

1) All plasma properties were found to be azimuthally symmetric beyond 1 mm downstream of the constrictor.

2) The temperature ratio T_{es}/T_g is much greater than unity in the near-anode region, so that a highly nonequilibrium plasma is present at the wall, requiring separate species energy equations for accurate simulation of the arcjet physics.

3) The propellant flow rate affects the axial location of maximum sheath potential, current density, and electron heating more than the arc current.

4) Most of the current density and anode heating occurs within 2–4 mm of the constrictor exit.

5) The electron power deposition into the anode accounts for ~18–24% of the total input power, increasing with mass flow rate. This suggests that anode loss decreases with decreasing $\dot{m}$.

6) The anode sheath potential is everywhere electron-attracting and accounts for over 50% of the anode heating; a weighted effective anode sheath potential varies between 8 and 17 V, depending on the thruster operating conditions.

7) Reasonable agreement between a numerical model and the experimental results was found, using an energy loss factor δ of 1200 in the model. This implies that a validated arcjet code can be used to predict anode power deposition at conditions of higher performance.

Acknowledgments

The authors acknowledge support by the U.S. Air Force Office of Scientific Research under Contracts F49620-92-J-0448 and -0280. Mitat Birkan was the Program Monitor. We gratefully acknowledge illuminating discussions with M. J. Kushner and D. Ruzic; critical assistance from W. Johnson, K. Elam, D. Foley, and J. Frizzell of the University of Illinois; advice and equipment support through T. Haag of NASA Lewis Research Center; and assistance in the laboratory from Ph.D. candidate G. Willmes.

References

[1]Tiliakos, N., "Plasma Properties and Heating at the Anode of a 1 kW Arcjet Using Electrostatic Probes," Ph.D. Dissertation, Dept. of Aeronautical and Astronautical Engineering, Univ. of Illinois at Urbana–Champaign, IL, 1997.

[2]Curran, F. M., and Haag, T. W., "Extended Life and Performance Test of a Low-Power Arcjet," *Journal of Spacecraft and Rockets*, Vol. 29, No. 4, 1992, pp. 444–452.

[3]Megli, T. W., Krier, H., and Burton, R. L., "Plasmadynamics Model for Nonequilibrium Processes in N_2/H_2 Arcjets," *Journal of Thermophysics and Heat Transfer*, Vol. 10, No. 4, 1996, pp. 554–562.

[4]Langmuir, I., and Mott-Smith, H. M., *General Electric Review*, Vol. 26, Nov. 1923, p. 731 and Vol. 27, July 1924, pp. 449, 583, 616, 726, 810; also *Physical Reveiw*, Vol. 28, No. 4, 1926, p. 727.

[5]Soulas, G. C., and Myers, R. M., "Mechanisms of Anode Power Deposition in a Low Pressure Free Burning Arc," NASA CR 194442, International Electric Propulsion Conf., Paper 93-194, Sept. 1993.

[6]Gallimore, A. D., Kelly, A. J., and Jahn, R. G., "Anode Power Deposition in Magnetoplasmadynamic Thrusters," *Journal of Propulsion and Power*, Vol. 9, No. 3, 1993, pp. 361–368.

[7]Carney, L. M., and Keith, T. G., "Langmuir Probe Measurements of an Arcjet Exhaust," *Journal of Propulsion and Power*, Vol. 5, No. 3, 1989, pp. 287–293.

[8]Burton, R. L., and Bufton, S. A., "Exit-Plane Electrostatic Probe Measurements of a Low-Power Arcjet," *Journal of Propulsion and Power*, Vol. 12, No. 6, 1996, pp. 1099–1106.

[9]Bufton, S. A., "Exit Plane Plasma Measurements of a Low-Power Hydrazine Arcjet," Ph.D. Dissertation, Dept. of Aeronautical and Astronautical Engineering, Univ. of Illinois at Urbana–Champaign, IL, 1996.

[10]Kim, S. W., Foster, J. E., and Gallimore, A. D., "Very-Near-Field Plume Study of a 1.35 kW SPT-100," AIAA Paper 96-2972, July 1996.

[11]Sankovic, J. M., "Investigation of the Arcjet Plume Near Field Using Electrostatic Probes," NASA TM 103638, Oct. 1990.

[12]Tan, W. P. S., "Transverse Cylindrical Probe in Plasma Diagnostics," *Journal of Physics D: Applied Physics*, Vol. 6, No. 7–12, 1973, pp. 1188–1205.

[13]Segall, S. B., and Koopman, D. W., "Application of Cylindrical Langmuir Probes to Streaming Plasma Diagnostics," *Physics of Fluids*, Vol. 16, No. 7, 1973, pp. 1149–1156.

[14]Hayes, D. T., and Rotman, W., "Microwave and Electrostatic Probe Measurements on a Blunt Re-Entry Vehicle," *AIAA Journal*, Vol. 11, No. 5, 1973, pp. 675–682.

[15]Bredfeldt, H. R., Scharfman, W. E., Guthart, H., and Morita, T., "Boundary-Layer Ion Density Profiles as Measured by Electrostatic Probes," *AIAA Journal*, Vol. 5, No. 1, 1967, pp. 91–98.

[16]Boyer, D. W., and Touryan, K. J., "Experimental and Numerical Studies of Flush Electrostatic Probes in Hypersonic Ionized Flows: I. Experiment," *AIAA Journal*, Vol. 10, No. 12, 1972, pp. 1667–1674.

[17]Russo, A. J., and Touryan, K. J., "Experimental and Numerical Studies of Flush Electrostatic Probes in Hypersonic Ionized Flows: II. Theory," *AIAA Journal*, Vol. 10, No. 12, 1972, pp. 1675–1678.

[18]Tseng, R. C., and Talbot, L., "Flat Plate Boundary-Layer Studies in a Partially Ionized Gas," *AIAA Journal*, Vol. 9, No. 7, 1971, pp. 1365–1372.

[19]Zube, D. M., and Myers, R. M., "Techniques for Spectroscopic Measurements in an Arcjet Nozzle," *Journal of Propulsion and Power*, Vol. 8, No. 1, 1992, pp. 254–256.

[20]Zube, D. M., and Auweter-Kurtz, M., "Spectroscopic Arcjet Diagnostic Under Thermal Equilibrium and Nonequilibrium Conditions," AIAA Paper 93-1792, June 1993.

[21]Glocker, B., and Auweter-Kurtz, M., "Numerical and Experimental Constrictor Flow Analysis of a 10 kW Thermal Arcjet," AIAA Paper 92-3835, July 1992.

[22]Hargus, W., Micci, M., and Spores, R., "Interior Spectroscopic Investigation of the Propellant Energy Modes in an Arcjet Nozzle," AIAA Paper 94-3302, June 1994.

[23]Curran, F. M., Manzella, D. H., and Pencil, E. J., "Performance Characterization of a Segmented Anode Arcjet Thruster," International Electric Propulsion Conf., Paper 90-2582, July 1990.

[24]Self, S. A., and Eskin, L. D., "The Boundary Layer Between Electrodes and a Thermal Plasma," *IEEE Transactions on Plasma Science*," Vol. P.S.-11, No. 4, 1983, pp. 279–285.

[25]Meeks, E., and Capelli, M. A., "A Multi-Fluid Model of Near-Electrode Plasma Behavior," AIAA Paper 93-2103, June 1993.

[26]Lichon, P., and Sankovic, J., "Development and Demonstration of a 600 Second Mission Average Arcjet," *Journal of Propulsion and Power*, Vol. 12, No. 6, 1996, pp. 1018–1025.

[27]Goodfellow, K. D., and Polk, J. E., "Experimental Verification of a High-Current Cathode Thermal Model," AIAA Paper 95-3062, July 1995.

[28]Clements, R. M., and Smy, P. R., "Sheath-Convection Effects with Flush-Mounted Electrostatic Probes," *Canadian Journal of Physics*, Vol. 49, May 1971, pp. 2540–2546.

[29]Thomas, T. L., and Battle, E. L., "Effects of Contamination on Langmuir Probe Measurements in Glow Discharge Plasmas," *Journal of Applied Physics*, Vol. 41, No. 8, 1971, pp. 3428–3432.

[30]Swift, J. D., and Schwar, M. J. R., *Electrical Probes for Plasma Diagnostics*, Elsevier, New York, 1969, pp. 220–245.

[31]Tiliakos, N. T., and Burton, R. L., "Arcjet Anode Sheath Voltage Measurement by Langmuir Probe," *Journal of Propulsion and Power*, Vol. 12, No. 6, 1996, pp. 1174–1176.

[32]Godyak, V. A., and Sternberg, N., "Smooth Plasma-Sheath Transition in a Hydrodynamic Model," *IEEE Transactions on Plasma Science*, Vol. 18, No. 1, 1990, pp. 159–171.

[33]Oberth, R. C., "Anode Phenomena in High-Current Discharges," Ph.D. Dissertation, Dept. of Mechanical and Aerospace Engineering, Princeton Univ., Princeton, NJ, 1970.

[34]Curran, F. M., "An Experimental Study of Energy Loss Mechanisms and Efficiency Considerations in the Low Power dc Arcjet," AIAA Paper 85-2017, Sept. 1985.

[35]Miller, S. A., and Martinez-Sanchez, M., "Two-Fluid Non-Equilibrium Simulation of Hydrogen Arcjet Thrusters," *Journal of Propulsion and Power*, Vol. 12, No. 1, 1996, pp. 112–119.

[36]Sutton, G. W., and Sherman, A., *Engineering MagnetoHydrodynamics*, McGraw–Hill, New York, 1965, pp. 148–190.

[37]Martinez-Sanchez, M., and Miller, S. A., "Arcjet Modeling: Status and Prospects," *Journal of Propulsion and Power*, Vol. 12, No. 6, 1996, pp. 1035–1043.